

AperTO - Archivio Istituzionale Open Access dell'Università di Torino

Formation of Reversible Adducts by Adsorption of Oxygen on Ce-ZrO₂: An Unusual 1•2 Ionic Superoxide

This is the author's manuscript

Original Citation:

Availability:

This version is available <http://hdl.handle.net/2318/1723926> since 2020-01-20T10:19:10Z

Published version:

DOI:10.1021/acs.jpcc.9b08615

Terms of use:

Open Access

Anyone can freely access the full text of works made available as "Open Access". Works made available under a Creative Commons license can be used according to the terms and conditions of said license. Use of all other works requires consent of the right holder (author or publisher) if not exempted from copyright protection by the applicable law.

(Article begins on next page)

The Formation of Reversible Adducts by Adsorption of Oxygen on Ce-ZrO₂: an Unusual η^2 Ionic Superoxide

Stefano Livraghi*^a, Maria Cristina Paganini^a, Elio Giamello^a,
Giovanni Di Liberto^b, Sergio Tosoni^b, Gianfranco Pacchioni^b

a) Dipartimento di Chimica and NIS, Università di Torino, Via P. Giuria 7, 10125 Torino, Italy.

b) Dipartimento di Scienza dei Materiali, Università Milano Bicocca, via R. Cozzi 55, 20125 Milano, Italy.

Stefano.livraghi@unito.it

Abstract.

The interaction of oxygen with Ce-ZrO₂ (Ce ions diluted in the Zirconia matrix) is a key aspect for many applications of this material. In this work, for the first time, an unusual reversible interaction of the O₂ molecule with the surface of this solid is reported. The joint use of Electron Paramagnetic Resonance (EPR) and Density Functional Theory (DFT) calculations has allowed a full description of the reversible O₂ adsorption phenomenon that involves a full electron transfer from Ce³⁺ centres to the adsorbed O₂ forming the superoxide anion (O₂^{•-}). The process can be completely reversed by removing the O₂ gas from the atmosphere as confirmed by the calculated values of both the adsorption energy (0.45 eV) and the activation energy (negligible) of the process. This behaviour is typical of a solid oxygen carrier. However, at variance of the reported cases of molecular and solid oxygen carriers that usually form η^1 end-on adducts, in the present case a side-on, η^2 Ce-O₂ surface complex is observed. Comparison of structural data and DFT results also indicates that Ce doping occurs in the lattice of tetragonal Zirconia while this is not observed in the monoclinic phase.

The Authors dedicate this paper to Prof. Michel Che (Université P. et M. Curie), a pioneer of the field of surface oxygen radicals who passed away on August 2019.

Keywords: Ce-ZrO₂, DFT, EPR, oxygen, reversible adsorption

1. Introduction

The redox couple Ce⁴⁺/Ce³⁺ plays a fundamental role in dictating the chemical and physical properties of Ce containing materials. In CeO₂ for instance, this ion pair enables this oxide to mimic different biological processes such as the typical reaction of superoxide dismutase (SOD) or the radicals scavenging.^{1,2} In CeO₂ and ZrO₂-CeO₂ mixed oxides it is also responsible for the high oxygen

storage capacity (OSC)³ which, in turn, is the basis of some important applications of these materials as in the three-way catalysts (TWC),^{4,5} carbon dioxide reforming of methane (CDRM),^{6,7} in water gas shift reaction (WGS)[8,9] and in the selective catalytic reduction (SCR) of NO.^{10,11}

Recently, investigating wide band gap semiconducting oxides doped with Ce ions, some of us have also shown that the redox couple $\text{Ce}^{4+}/\text{Ce}^{3+}$ is involved in the phenomenon of the reversible O_2 adsorption, via superoxide ($\text{O}_2^{\bullet-}$) species formation,^{12,13} a process relevant in different research areas such as the oxygen transport in biological systems, the selective adsorption and separation of gas mixtures, or catalytic processes. This phenomenon is commonly reported for inorganic or biological compounds,^{14,15} but examples involving metal oxides are also known.¹⁶⁻¹⁸

As far as Ce containing oxides are concerned, reversible oxygen adsorption has been observed for $\text{CeO}_2\text{-TiO}_2$ and Ce-doped ZrTiO_4 . As for the bare Cerium dioxide, the reversible formation of the superoxide species ($\text{O}_2^{\bullet-}$) was also reported in the past.^{19,20} This result, however, is not totally unambiguous. The observed phenomenon seems to concern only a fraction of the whole oxygen interaction and is not mentioned in successive work about the $\text{O}_2\text{-CeO}_2$ interaction.²¹ In the case of the two mixed oxides, $\text{CeO}_2\text{-TiO}_2$ and Ce-ZrTiO_4 , the origin of the reversible O_2 adsorption is due to presence of Ce^{3+} centres. In the case of $\text{CeO}_2\text{-TiO}_2$ the mutual solubility of the two parent oxides is very low and the presence of Ce^{3+} is related to the formation of an interfacial $\text{Ce}_2\text{Ti}_2\text{O}_7$ pyrochlore phase along the synthesis of the material.¹² In the case of Ce-ZrTiO_4 where the two parent oxides (CeO_2 and ZrO_2) form solid solutions, the Ce^{3+} ions responsible for the reversible O_2 adsorption in the form of superoxide ion ($\text{O}_2^{\bullet-}$) are distributed in the oxide lattice.¹³

Considering that in the above-mentioned applications the balance between the oxygen storage and release capacity represents a key aspect, any new insight concerning the O_2 interaction with this kind of materials can contribute to better understand the involved catalytic mechanisms.

In this paper we report a description of the reversible adsorption of oxygen in form of superoxide anion on cerium centres at the surface of Ce-doped zirconium dioxide. The interaction has been monitored by Electron Paramagnetic Resonance, the reference technique to investigate surface oxygen paramagnetic species often not detectable by vibrational spectroscopies. Due to the peculiarity of this phenomenon (in most cases the superoxide is the initial step of a progressive reduction and incorporation of oxygen into the oxide lattice) a parallel computational investigation of the system is essential to validate the proposed model. We have therefore selected the case of Ce-ZrO₂ (less complex than the two systems mentioned before^{12,13}) to develop, in parallel to the experiments, advanced DFT calculations aimed at thoroughly describe the nature of this surface interaction.

As it will be shown in the following, the synergies between EPR and DFT have been crucial to describe the features of a phenomenon whose importance is not only related to a specific and unusual type of surface to molecule bonding, but that could have also, in perspective, appealing applications in the area of oxygen transport and oxygen separation from gas mixtures.

2. Materials and Methods

2.1) Sample preparation.

Pure ZrO₂ and Ce doped ZrO₂ samples, with a nominal loading of 0.5, 1, 8 and 10 Ce molar percentage were prepared via hydrolysis of zirconium propoxide. The samples are identified by the abbreviation CeXZ where X indicates the cerium loading (05 is for 0.5). In a typical synthesis the zirconium propoxide (70% w/w in 1-propanol) were previously diluted in an equal volume of alcohol (2-propanol) and then hydrolysed with water using a volume ratio, between zirconium propoxide and water, equal to 2.9. In the case Ce-doped ZrO₂, CeCl₃•7H₂O was employed as dopant source and beforehand dispersed in the water employed for the synthesis. The obtained solids were dried at 343 K and finally calcined at 973 K for one hours.

2.2) Sample characterization.

Powder X-ray diffraction (XRD) patterns were recorded with a PANalytical PW3040/60 X'Pert PRO MPD diffractometer using a copper K α radiation source and the X'Pert High-Score software was used for data handling. Diffraction patterns were refined with Rietveld method using MAUD (Material Analysis Using Diffraction) program.^{22,23} Continuous Wave Electron Paramagnetic Resonance (CW-EPR) experiments were performed with a Bruker EMX spectrometer operating at X-band (9.5 GHz), equipped with a cylindrical cavity operating at 100 kHz field modulation. Spectra at 77K were obtained keeping the sample in liquid nitrogen using a finger Dewar set in the EPR cavity.

2.3) O₂ adsorption.

All the O₂ adsorption experiments were performed in EPR cells that can be connected to conventional high-vacuum apparatus (residual pressure < 10⁻⁴ mbar). O₂ adsorption was carried out after an activation process performed in order to get rid of all contaminants adsorbed on the surface according to the following procedure. An initial thermal annealing in vacuum at 773K for 30 minutes was followed by an oxidation step again at 773K for 60 minutes under 20 mbar of O₂.

For all the experiments 2 mbar of oxygen was dosed in the EPR cell at room temperature and then the temperature was lowered to 77K by immersion in liquid nitrogen. For the isotopically enriched oxygen, ¹⁷O₂ (90% atoms) was employed. The EPR spectra, except otherwise indicated, were recorded at 77K.

2.4) Computational details.

We performed calculations at the DFT level using the Plane Wave Code VASP.²⁴⁻²⁷ Projector Augmented Wave (PAW)²⁸ pseudopotentials have been adopted, and the calculations account for spin polarization. The Perdew-Burke-Ernzerof (PBE) exchange-correlation functional has been adopted.²⁹ The energy basis cutoff was set to 400 eV, and the optimizations were performed using the conjugate gradient scheme until the change in total energy between successive steps was less

than 10^{-5} eV and residual forces were below 0.01 eV/Å. The Ce 4f states are described according to the DFT+U³⁰ approach by setting the U parameter for Ce 4f states to 4 eV.³¹⁻³³ The same value, U = 4 eV, is also applied to Zr 3d states.³⁴ The sampling in the reciprocal space has been restricted to Gamma (Γ) point due to the cells size.

We simulated clean and Ce-doped tetragonal and monoclinic ZrO₂ bulk phases. The lattice parameters and ionic coordinates determined experimentally^{35,36} have been adopted to build up the supercells in order to have a realistic doping ratio. We adopted a 3x3x3 expansion of tetragonal ZrO₂, and 3x2x2 of the monoclinic phase. Both models contain a comparable number of atoms, made by (ZrO₂)₅₄ and (ZrO₂)₄₈ units, respectively. We fully optimized both the lattice and the atomic coordinates. The results of the pristine and doped models, with one or two substitutional Ce atoms, are reported in Table 1.

In a second step, in order to investigate the O₂ interaction with the surface of the Ce doped materials, we simulate a model made by the (101) surface of tetragonal ZrO₂, starting from previous work.³⁴ The model is made by (ZrO₂)₆₀ units, and the cell vectors *a* and *b* are 11.048 Å and 12.855 Å, respectively. We added a vacuum region of roughly 20 Å to ensure that negligible interaction occurs between periodic replica of the system around the non-crystallographic direction. Dispersion interactions have been accounted in the model by employing the D2' scheme.³⁷

3. Results

3.1. Structural characterization

Ce-ZrO₂ samples show the presence of two zirconia polymorphs, the monoclinic and the tetragonal phase respectively (Table 1, experimental data). It is worth to mention that the strong similarity between the diffraction patterns of the tetragonal and the cubic phases as well as the broadening of the observed diffraction peaks usually makes it difficult to clearly establish, based on visual

analysis, whether the second phase is actually tetragonal or cubic.^{38,39} However a Rietveld refinement of the experimental patterns indicates the presence, beside monoclinic zirconia, of the tetragonal one.^{7,40} The absence of any evidence of CeO₂ diffraction peaks even in the case of high loading materials confirms that a solid solution containing cerium ions in the cation sub-lattice is formed (Figure 1).

The insertion of Ce ions in the ZrO₂ bulk induces a significant modification of the lattice parameters of the oxide proportional to the Ce loading. This occurs, however, in the case of the tetragonal polymorph only, while the monoclinic structure seems unaffected (Figure 2). The presence of cerium also modifies the ratio between the two polymorphs increasing the percentage of the tetragonal phase according to an evidence already reported in the literature.⁴¹

	Sample	Ce (%mol)	Polymorph	Abund. (%w/w)	$a(\text{Å})/(\Delta\%)$	$b(\text{Å})/(\Delta\%)$	$c(\text{Å})/(\Delta\%)$
Experimental	ZrO ₂	0	Tetr.	36	3.6043/(0.0)	3.6043/(0.0)	5.1772/(0.0)
			Mon.	64	5.1633/(0.0)	5.2006/(0.0)	5.3244/(0.0)
	Ce05Z	0.5	Tetr.	41	3.6073/(0.08)	3.6073/(0.08)	5.1834/(0.12)
			Mon.	59	5.1587/(-0.09)	5.2051/(0.09)	5.3261/(0.03)
	Ce1Z	1	Tetr.	38	3.6134/(0.25)	3.6134/(0.25)	5.1910/(0.27)
			Mon.	62	5.1598/(-0.07)	5.2054/(0.09)	5.3266/(0.04)
	Ce8Z	8	Tetr.	70	3.6327/(0.79)	3.6327/(0.79)	5.2176/(0.78)
			Mon.	30	5.1557/(-0.15)	5.2039/(0.06)	5.3319/(0.14)
	Ce10Z	10	Tetr.	82	3.6331/(0.80)	3.6331/(0.80)	5.2161/(0.75)
			Mon.	18	5.1593/(-0.08)	5.2108/(0.20)	5.3265/(0.04)
Calculated	ZrO ₂		Tetr.		3.6300/(0.0)	3.6300/(0.0)	5.1679/(0.0)
			Mon.		5.1914/(0.0)	5.2752/(0.0)	5.3325/(0.0)
	Ce ^b -ZrO ₂		Tetr.		3.6334/(0.09)	3.6334/(0.09)	5.1678/(0.0)
			Mon.		5.1994/(0.15)	5.2799/(0.09)	5.3385/(0.11)
	Ce ^{bb} -ZrO ₂		Tetr.		3.6371/(0.19)	3.6371/(0.19)	5.1722/(0.08)
			Mon.		5.2047/(0.26)	5.2870/(0.22)	5.3382/(0.11)

Table 1: The experimental section reports the abbreviations, phase composition and lattice parameters obtained via Rietveld refinement of the XRD patterns of the ZrO₂ and Ce-ZrO₂ materials. The computational section reports lattice parameters of ZrO₂ and Ce-ZrO₂. Ce^b-ZrO₂ is for Ce-doped model with both one atomic dopant, Ce^{bb}-ZrO₂ is for Ce-doped model with two atomic dopants. Real samples are instead labelled as Z for pristine material, and X for Ce-doped with X% dopant concentration. Values in parenthesis are the % deviations ($\Delta\%$) with respect to pure models/samples.

Table 1 reports the calculated lattice parameters of tetragonal and monoclinic ZrO₂ for the bare and doped oxides at the DFT level. Two different models of Ce-doped ZrO₂ have been considered,

involving one or two Ce ions in the supercell, roughly corresponding to a molar fraction of about 2% and 4%, respectively. In the case of the tetragonal phase the calculated lattice vectors of the pristine ZrO_2 crystal are in good agreement with the experimental values, being the deviations 0.8% and 0.2% for a and c directions, respectively. In the case of doped materials, considering a dopant concentration of 1% (C1Z), the experimental lattice parameters are larger by 0.25% and 0.27% than those of the unperturbed oxide, while for a dopant loading one order of magnitude higher (C10Z), the two values increase by 0.80% and 0.75%. The calculated model is in quite good agreement with the previous data. Indeed, at various Ce concentrations (one or two Ce atoms in the supercell) a lattice expansion of 0.09% and 0.0% (one Ce), and 0.19% and 0.08% (two Ce), respectively, has been observed.

Moving to monoclinic ZrO_2 , the experimental and calculated lattice parameters of the undoped material are very similar, with deviations equal to 0.5 %, 1.4%, and 1.3%, for a , b , and c respectively. Differently from the previous case of the tetragonal phase, however, the significant deviations from the unperturbed lattice parameters forecast by theoretical calculations (even more pronounced than in the case of the tetragonal phase) are not observed by X-ray diffraction data. In fact, the experimental lattice parameters of monoclinic doped samples (Table 1) are almost insensitive to Ce loading. This result may be rationalized by assuming that, in real samples, Ce doping selectively occurs for the tetragonal phase only.

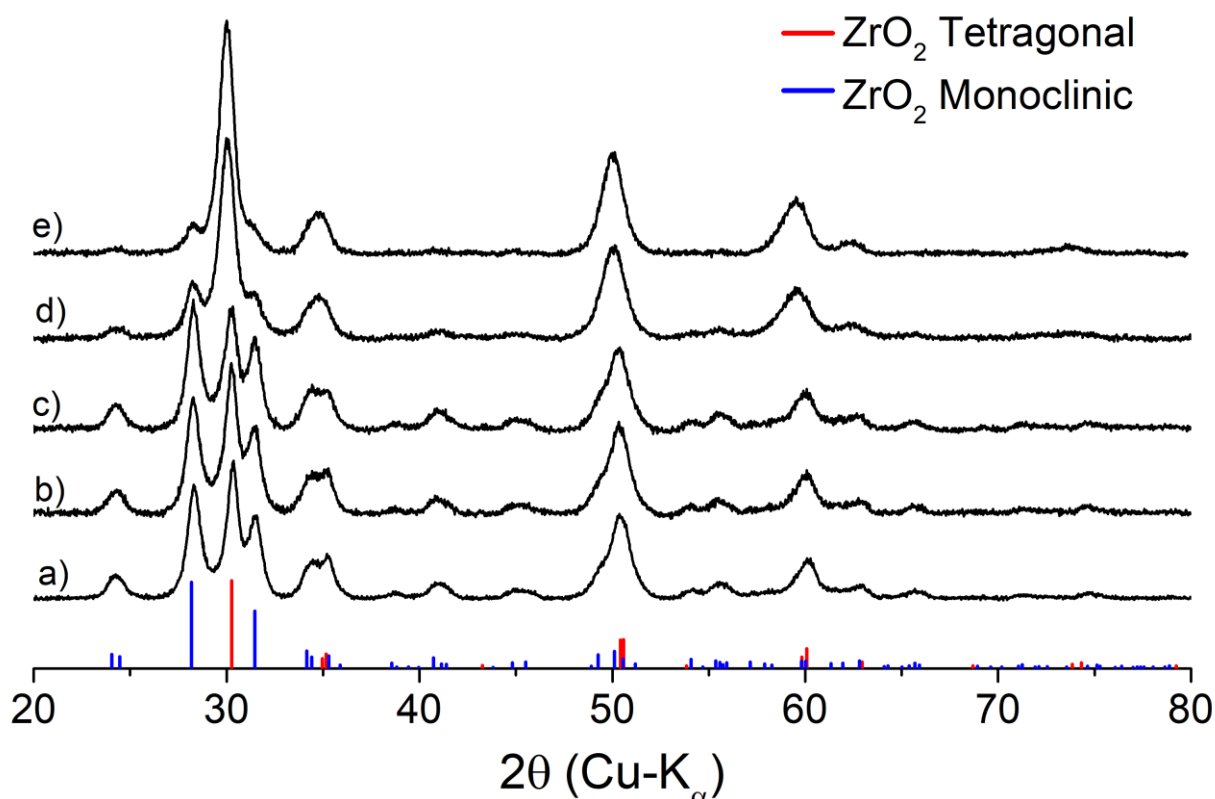


Figure 1: XRD patterns of bare and Ce containing ZrO_2 samples. a) ZrO_2 , b) Ce0.05Z, c) Ce0.1Z, d) Ce0.2Z and e) Ce0.3Z. In the lower part of the figure the red and blue patterns indicate the XRD reflections for the tetragonal and monoclinic structure respectively.

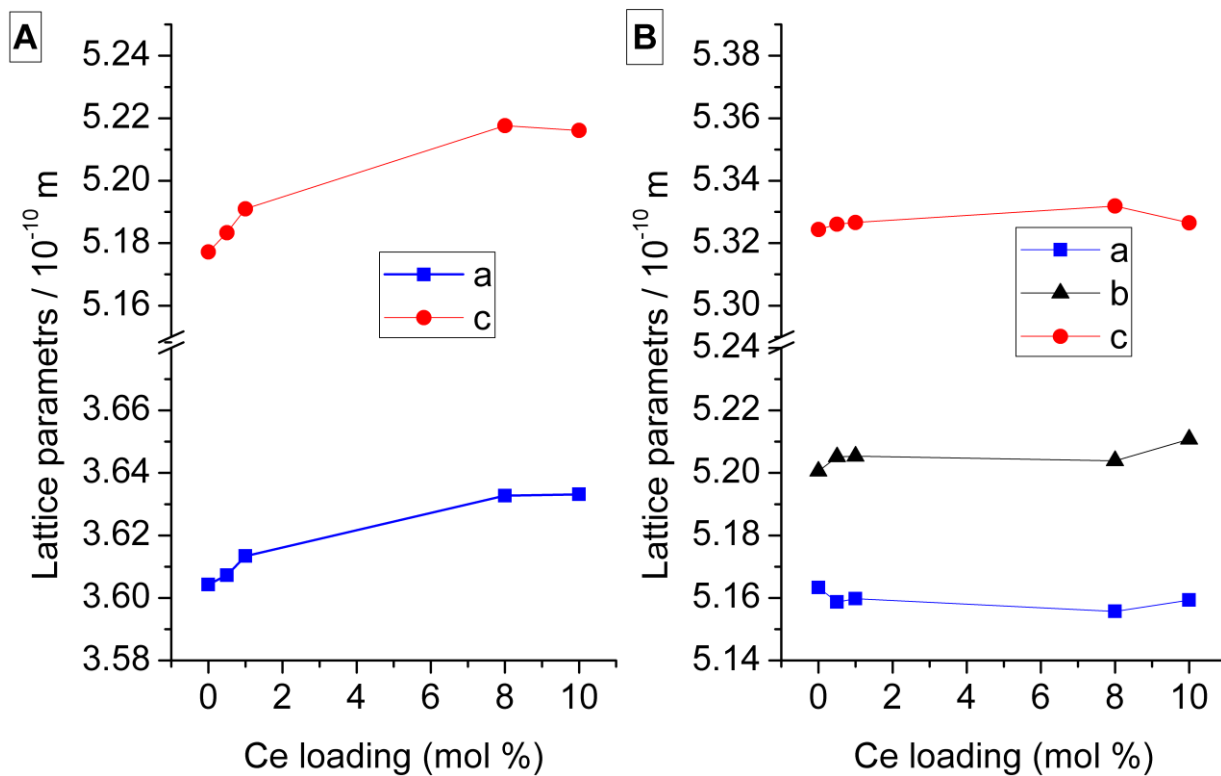
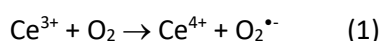


Figure 2: Lattice parameters obtained via Rietveld refinement of the XRD patterns of the ZrO_2 samples. Panel A: Lattice parameters (a and c) of the tetragonal phase. Panel B: Lattice parameters (a, b and c) of the monoclinic phase.

3.2. EPR Evidence of reversible O₂ adsorption as O₂^{•-} superoxide ion

The as-prepared materials, prior the activation via thermal treatment as described above, do not react with molecular oxygen. After the activation treatment, the EPR spectrum of Ce-doped materials is nearly flat except for a weak signal due to a tiny amount of bulk Zr³⁺ intrinsic defects (Fig. 3A spectrum a). Contacting the activated materials with O₂, the formation of a paramagnetic species occurs whose EPR spectrum (Fig. 3A spectrum b) is assigned to a superoxide species adsorbed on tetravalent Ce ions (Ce⁴⁺-O₂^{•-} adduct) as definitely indicated by the observed g values (see Table 2). Such EPR signal is strictly similar to that observed in the case of the Ce-ZrTiO₄ and CeO₂-TiO₂ systems^{12,13} and definitely differs from that reported in the case of superoxide ions generated on pure cerium dioxide which is characterized by a higher g_{zz} value.¹²

The easy formation of a paramagnetic species on a solid that underwent an oxidative treatment at the end of the activation process can be explained assuming that reduced centres are still present in the solid despite the mentioned oxidation. Since the superoxide anion forms on top of Ce⁴⁺ ions the reaction occurring at the surface can be written as:



We thus assume (see discussion Section) that trivalent cerium ions are present at the surface of activated Ce-ZrO₂.

The stability of the O₂^{•-} species on Ce-ZrO₂ is strictly dependent on the O₂ pressure as shown in Figure 3A and 3B, that refer to the C10Z material. The O₂^{•-} EPR signal, in fact, disappears after O₂ outgassing at room temperature (Fig 3A spectrum c). Dosing again O₂, the superoxide species is restored (Fig. 3A spectrum d) and again it vanishes by outgassing (spectrum e). Figure 3B reports the intensity of the superoxide species, obtained via double integration of the related EPR signals, as a function of the O₂ partial pressure. Such a dependence can be tested only for a limited range of O₂ pressure (0-8 mbar) because the dipolar broadening effects occurring at higher O₂ pressure

(molecular oxygen is a $S=1$ spin system) affects the intensity of the superoxide signal. Figure 3B indicates that the EPR signal intensity is proportional to the amount of O_2 dosed in the experiment. The reversibility of the O_2 adsorption process is also observed at temperatures lower than RT even though, in these conditions, the desorption rate upon outgassing decreases. The O_2 outgassing performed for 15 minutes at about 150K (figure 3A spectrum f) in fact induces a significant decrease of the $O_2^{\bullet-}$ EPR intensity (always measured at 77K for the sake of comparison). The observed abundant desorption upon pumping off at 150K therefore indicates that the activation energy for the desorption process is very low in agreement with the computational output (see section 3.5.1).

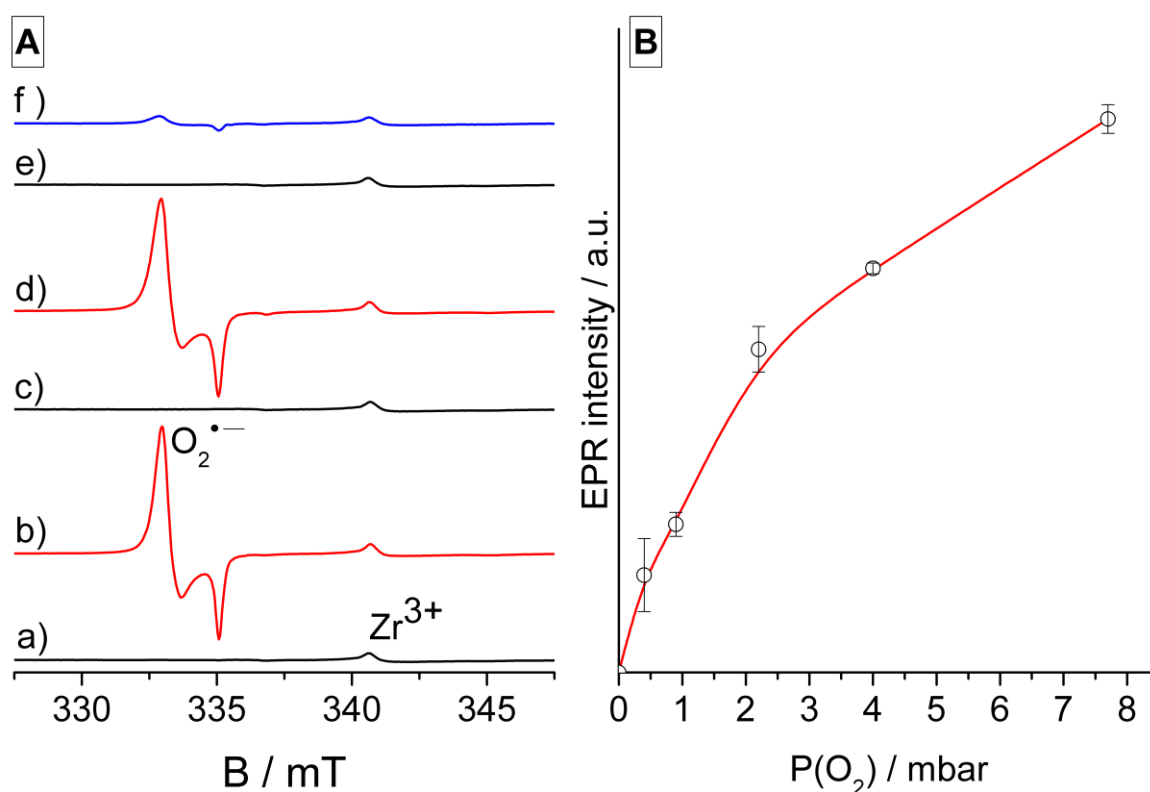


Figure 3: A) EPR spectra recorded at 77K showing the reversible formation of the superoxide species on Ce10Zr. a) material under vacuum, b) in presence of 2 mbar of O_2 , c) after outgassing at RT, d) after re-adsorption of 2 mbar of O_2 , e) again outgassed at RT, f) outgassed at 150K for 15 minutes. B) Pressure dependence of the EPR intensity of the superoxide species detected via EPR).

3.3. EPR parameters, geometry and spin density of adsorbed superoxide

The EPR signal obtained dosing ^{17}O enriched O_2 (90% enrichment) in the same conditions of Fig. 3 produces the spectrum of Fig. 4, whose rich hyperfine structure (^{17}O , $I=5/2$) is essentially based on a set of 11 equi-separated lines with intensity ratio 1:2:3:4:5:6:5:4:3:2:1 centred on the g_{yy} component. This set of 11 lines is due to the ^{17}O - ^{17}O isotopomer and firmly indicates the magnetic (hence structural) equivalence of the two oxygen atoms of the superoxide species, which suggests a η^2 side-on structure with the radical anion symmetrically adsorbed on top of the Ce ion.

The spectra in Fig. 3 and 4 allow to determine the principal values of both \mathbf{g} and $\mathbf{A}(^{17}\text{O})$ tensors of the superoxide species. These are reported in Table 2 where we have adopted the convention, used in similar cases, $g_{zz} > g_{yy} > g_{xx}$. The species here described differ from the large majority of the surface superoxide ions adsorbed on oxides⁴² that usually follow an ionic model described years ago in a seminal paper by Kanzig and Cohen.⁴³ The differences are two: a) all three principal values of the \mathbf{g} tensor are higher than the free spin value, $g_e = 2.0023$ ($g_{zz} > g_{yy} > g_{xx} > g_e$) while in the ionic model $g_{zz} > g_{yy} > g_{xx} = g_e$ is the expected sequence; b) the largest ^{17}O hyperfine coupling is along the y direction (we assume here as reasonable the coincidence of the \mathbf{g} and \mathbf{A} principal axis) while in the ionic case it is along the x axis of the tensor.

These two peculiar features suggest that the $\text{Ce-O}_2^{\bullet-}$ interaction is affected by some degree of covalency even though the high value of the spin-orbit coupling constant for Ce could be also responsible of the deviation described at point a). Covalent interaction has been observed in several cases of oxygen adducts on transition metal ions [16, and references therein] which exhibit, however, an η^1 structure end-on bonded to the metal centre. The present case looks somehow analogous to that described by Pietrzyk et al.⁴⁴ concerning the Ni-superoxide adduct in MFI zeolites that shows a symmetric side-on structure and an essentially covalent interaction as indicated, *inter alia*, by the high deviations of all the element of the \mathbf{g} tensor from the free electron value ($\Delta g_{ii} = g_{ii}$

$-g_e$). In the present case, this difference is much less pronounced indicating a lower level of covalent interaction, as also suggested by the small binding energy revealed by the reversibility of the adsorption.

Simulation of the ^{17}O hyperfine structure (Fig. 4) allows to obtain the full hyperfine matrix (Table 1). The signs of the three diagonal elements have been chosen in agreement with similar cases.⁴³⁻⁴⁵ The non-negligible uncertainty on the two smaller components of the hyperfine tensor (Table 1) limits the exact decomposition of the matrix in the various contributions as done for instance in ref. 45. However, comparing the approximate experimental a_{iso} and b values with the corresponding atomic values ($A^\circ=166.0$ mT, $B^\circ= 5.15$ mT), the spin density (ρ) on the adsorbed superoxide ion can be evaluated to be higher than 0.9, in agreement with the idea of a nearly complete surface-to-molecule electron transfer as well as with the computational output (see Section 3.5.1.)

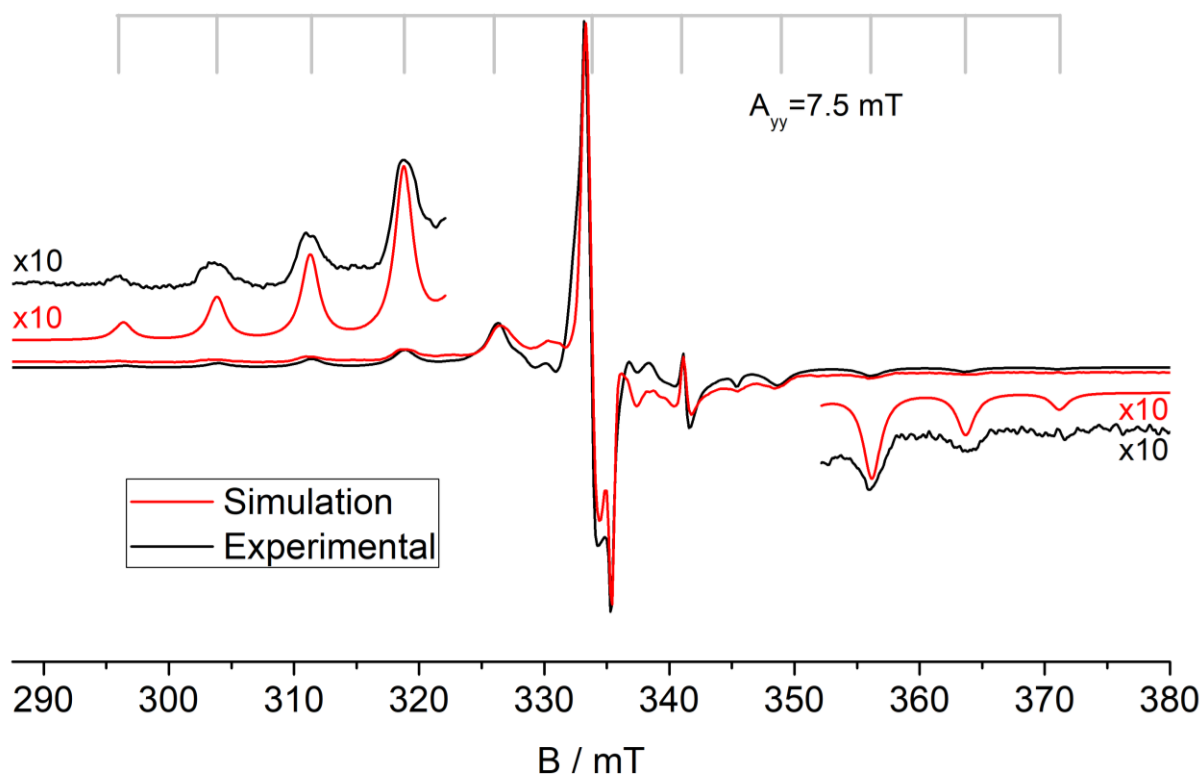


Figure 4: Experimental and simulated EPR spectra of Ce0.5-ZT sample contacted with $^{17}\text{O}_2$ (90% atoms).

substrate	g_{zz}	g_{yy}	g_{xx}	$^{17}\text{O Azz}$ (mT)	$^{17}\text{O Ayy}$ (mT)	$^{17}\text{O Axx}$ (mT)	ref.
Ce-ZrO₂	2.026	2.022	2.013	0.8±0.2	-7.5±0.05	1.6±0.4	This work
Ce-ZrTiO₄	2.026	2.03	2.013	~ 0	7.6	~ 0	13
CeO₂-TiO₂	2.025	2.021	2.013	unresol.	7.5	unresol.	12
CeO₂-TiO₂	2.026	2.021	2.013	unresol.	7.6	unresol.	12

Table 2: Spin Hamiltonian parameters of the superoxide species obtained on Ce-ZrO₂ compared with those obtained on other Cerium containing materials.

To resume, oxygen adsorption spontaneously occurs on activated Ce-ZrO₂ materials without the need of a preliminary generation of excess electrons in the solid, for instance via thermal annealing in vacuum. O₂ is adsorbed under the form of superoxide ion with an effective degree of surface-to-oxygen electron transfer mitigated by some relatively minor degree of covalent interaction. The adsorption is pressure dependent and the solid system thus behaves as a heterogeneous (i.e. non molecular) oxygen carrier even if the structure of the adduct is symmetric (η^2 side-on). Molecular⁴⁶ or heterogeneous¹⁶ oxygen carriers in fact usually exhibit an end-on η^1 structure. The side-on structure is typical of many ionic superoxide adducts observed at the surface of metal oxides that, however, are usually strongly bound to the surface and are stable upon pumping at room temperature or further react at higher temperature. The Ce-ZrO₂ system, together with the analogous Ce-ZrTiO₄, represents, to the best of our knowledge, the first example of heterogeneous oxygen carrier with η^2 side-on structure.

3.4. Role of the Ce oxidation state on the reversible O₂ adsorption

The amount of adsorbed superoxide species monitored, in the present work, strictly depends on the Ce loading and on the reduction state of the solids. Figure 5A compares the EPR spectra obtained, on Ce05Z and Ce10Z samples, via O₂ contact in the same conditions of Fig. 2. The signal is higher in the case of Ce10Z indicating that the O₂^{•-} amount is proportional to the Ce loading. Figure 5B shows the EPR signal of the O₂^{•-} species still generated on Ce10Z in the case of the activated materials

(signal a, black spectrum) and after thermal reductive annealing in vacuum for 60 minutes at 373K and 473K (spectra c and d, respectively). Data obtained by double integration of the spectra (inset in figure 5B) clearly indicate that, after annealing, the amount of $O_2^{\bullet-}$ species generated via O_2 adsorption increases. Such behaviour can be explained considering that upon annealing at high temperature the oxide matrix (ZrO_2) loses oxygen leaving excess electrons in the solid. The electrons, in turn, reduce the Ce ions from +4 to +3 causing the observed phenomenon (reaction 1).

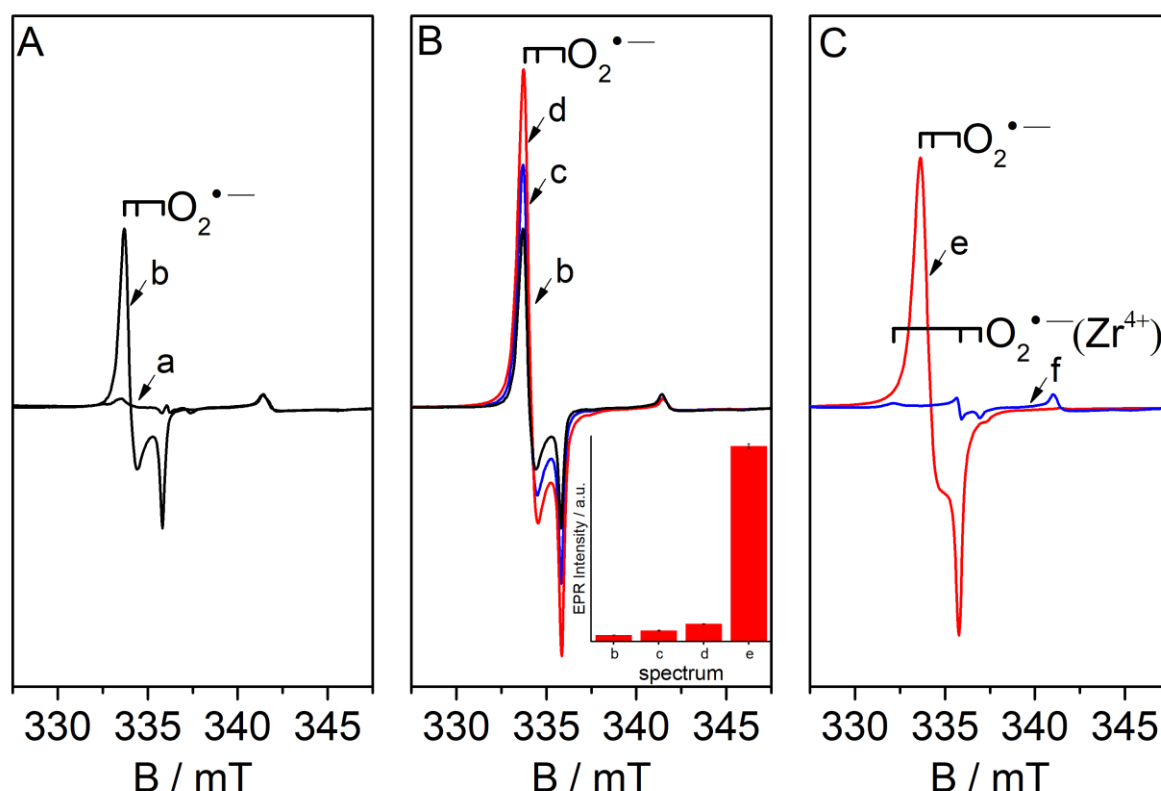


Figure 5: Panel A, $O_2^{\bullet-}$ species formed via contact of 2 mbar of O_2 on a) Ce05Z and b) Ce10Z. Spectra recorded at 77K. Panel B, $O_2^{\bullet-}$ species formed via contact of 2 mbar of O_2 on Ce10Z (spectrum b, same of panel A) and after progressive thermal annealing at 373K (c) and 473K (d) for 1h. Panel C, $O_2^{\bullet-}$ species formed via contact of 2 mbar of O_2 on Ce10Z previously annealed at 673K (spectrum e) and after outgassing the oxygen reversible fraction (spectrum f). The inset in Panel B reports the EPR intensity obtained by double integration of the spectra b, c, d and e.

Even in the cases of the sample annealed at 373K and 473K the O_2 outgassing causes the disappearing of the $O_2^{\bullet-}$ species. A different behaviour is instead observed after annealing at higher temperature. Increasing the temperature up to 673K induces the formation of a higher amount of $O_2^{\bullet-}$ species as expected, but in this case, evacuation of reversibly adsorbed O_2 evidences the

presence of a new stable signal which does not vanish upon prolonged outgassing (spectrum f in Figure 5C). The new signal is characterized by the following g values, $g_1=2.032$, $g_2=2.010$ and $g_3=2.003$ and correspond to a $O_2^{\bullet-}$ species, in this case adsorbed on Zr^{4+} ions as commonly observed for ZrO_2 .⁴⁷

3.5. O_2 adsorption via theoretical calculations

We modelled the Ce doped samples by including in the ZrO_2 lattice two substitutional Ce atoms, both having a formal oxidation state +4. Then, we generated reduced Ce species by creating a specific point defect in our model, an oxygen vacancy in the bulk of the structure. In the optimized system, the two excess electrons associated to the O vacancy reduce the two Ce dopants according to the process $Ce^{4+} + e^- \rightarrow Ce^{3+}$.

In ZrO_2 (101) models we have therefore two Ce^{3+} ions that originate from the creation of one oxygen vacancy in the supercell. We investigated three different models, all having one Ce^{3+} buried in the bulk, and the second Ce^{3+} species (1) in a surface layer, (2) in a bulk-like layer, and (3) in a subsurface layer, which represent an intermediate situation between (1) and (2). Comparing the three models, the Ce dopant is energetically favored when replaces a Zr ion on the surface layer. This configuration is 1.2 eV more stable than those with Ce^{3+} in the sub-surface and bulk layers of the slab, that are almost isoenergetic ($\Delta E = 0.04$ eV). This suggests that during calcination migration of Ce ions from the bulk to the surface can occur. The spin density on each dopant is almost equal to one (0.98 and 0.96).

3.5.1. O_2 adsorption: Ce^{3+} species in the bulk and in the surface layer of tetragonal ZrO_2 (101)

Two stable adducts, with a total energy below that of separated moieties, are formed (the minus sign indicates a bound system). In the first adduct O_2 is physisorbed with a binding energy of -0.27 eV, while the second one corresponds to the chemisorption of O_2 on top of the surface. This state

has a binding energy of -0.45 eV. The chemisorption of O₂ induces an electron transfer from Ce³⁺ to O₂ according to reaction 1.

Figure 6 shows the one-dimensional potential energy profile as a function of the Ce-O₂ distance. For each point we optimized the atomic coordinates by keeping fixed the z-atomic coordinates of Ce and O₂. Starting from long distances we recognize a typical long-range attractive region that reaches a local minimum at 3.10 Å, corresponding to a physisorption state, in which both molecular oxygen and Ce³⁺ retain their geometric and electronic structures. Indeed, the O-O distance is 1.27 Å to be compared with 1.25 Å for isolated O₂. Moving to shorter distances, the physisorption adduct is separated from the chemisorption one (at -0.45 eV) by an energy barrier. This state is associated to an effective charge transfer between Ce³⁺ and O₂. The height of the barrier is about 0.30 eV. This rather high value, compared to the adsorption energy of the physisorbed species, is also due to the geometrical constraints enforced to the oxygen molecule in this one-dimensional scheme: namely, at each point of the plot the energy is calculated by keeping the Z coordinate of O₂ fixed, thus forcing the molecule in a perfectly flat arrangement. Local relaxation effects may indeed reduce the energy barrier separating physisorbed and chemisorbed species.

The formation of a superoxide ion on top of the surface induces an increase of the O-O bond length, that moves from 1.25 Å to 1.33 Å. At the same time, the surface Ce atom reduces its spin population from 0.98 to 0.04. The electron is transferred to O₂, and the total spin of the resulting O₂^{•-} ion is 0.86, very close to the ideal value 1 and in perfect agreement with the experimental evidence (Section 3.3). Both oxygen atoms are magnetically equivalent. Moreover, the configuration of the oxygen atoms is that of a side-on arrangement on the surface Ce species. These results reproduce well the experimental evidences. The calculated properties of O₂^{•-} on top of the surface Ce dopant are also in agreement with previous calculations on O₂^{•-} on top of CeO₂ (O-O distance 1.33 Å, to be compared with 1.34 Å of Ref. 48, and total spin on O₂^{•-} 0.86 to be compared with 0.85 of Ref. 48).

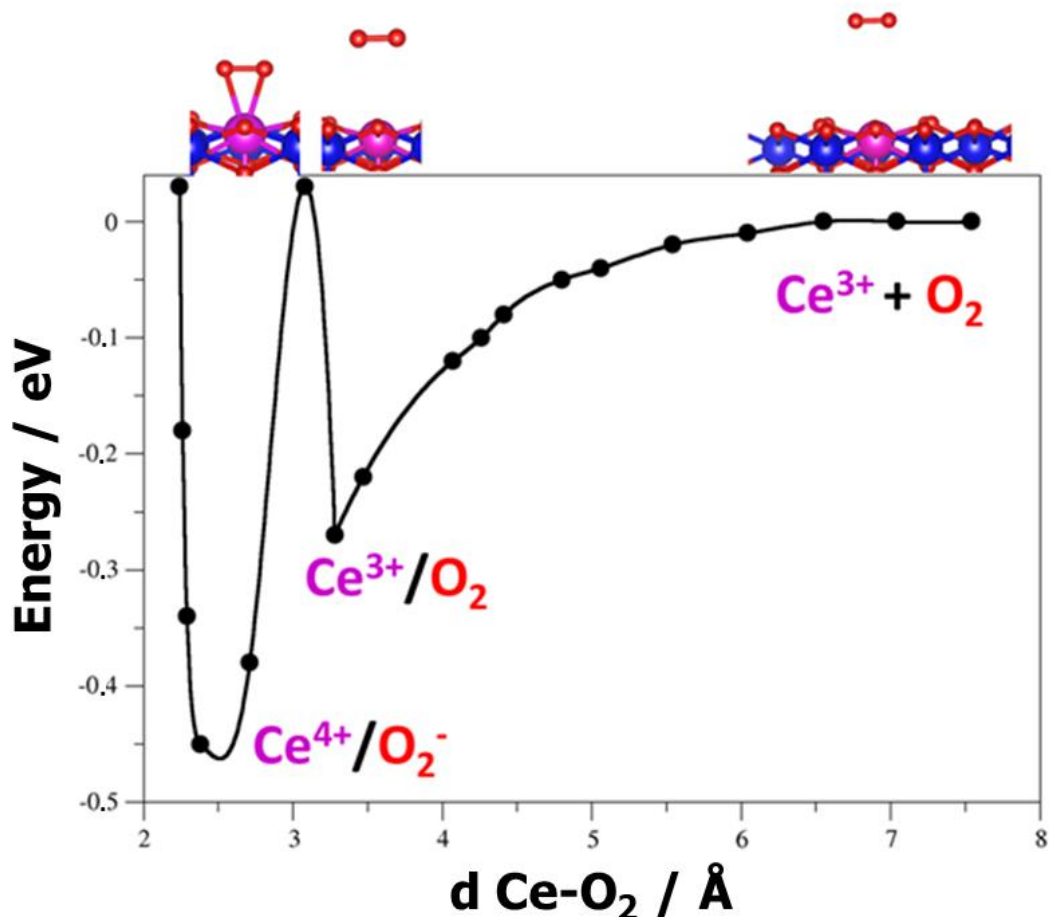


Figure 6: Potential energy profile as a function of the Ce-O₂ distance, in Å. Energies are in eV. The zero in energy has been set at separated Ce-doped ZrO₂ and O₂ units. The global minimum corresponds to the state where an electron transfer occurred, leading to Ce⁴⁺ and O₂⁻. The local minimum corresponds to O₂ physisorption to the surface. Magenta: Ce; red: O; blue: Zr.

Figure 7 reports the structure of the most stable adduct associated to the formation of the superoxide ion. One can see that the interaction with O₂ causes a shift by 0.5 Å of the Ce⁴⁺ ion outward the atomic layer associated to surface Zr⁴⁺ ions.

One can then look at the energetics of O₂^{•-} adsorbed on different sites, surface Ce dopant, or Zr⁴⁺ ions. In the latter case the adduct has a binding energy of -0.65 eV, lower than -0.45 eV found for surface Ce³⁺ species. A possible explanation for this result is that upon formation at room temperature of the adduct and consequent cooling, a significant energy barrier is present for the migration of O₂^{•-} from surface Ce⁴⁺ ions to Zr⁴⁺ ones, since the separation of O₂ from Ce is an activated process (Figure 6).

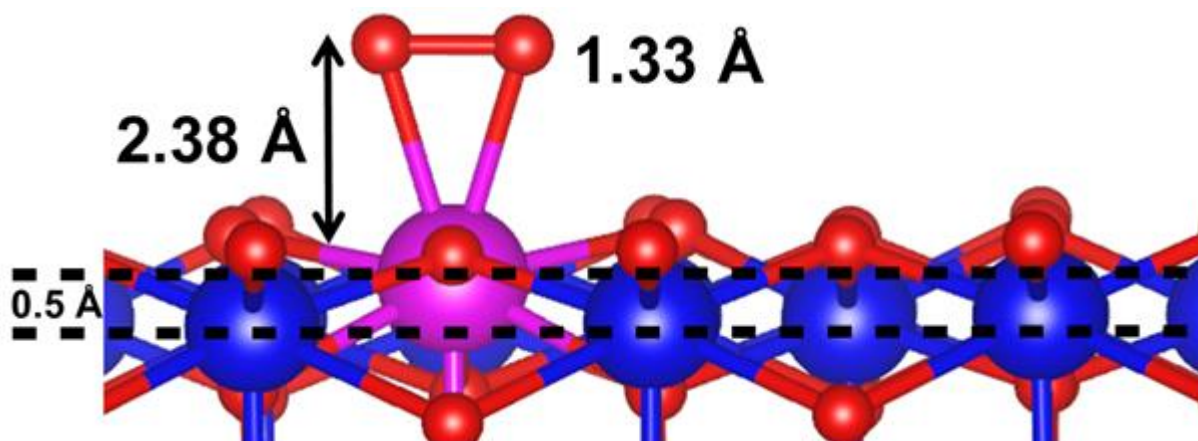


Figure 7: Optimized model of Ce-doped (101) ZrO_2 surface interacting with O_2 . The dashed lines indicate the non-crystallographic "z" coordinated of surface layer Zr^{4+} and Ce^{3+} ions. Magenta: Ce; blue: Zr; red: O.

3.5.2) O_2 adsorption: two Ce^{3+} species in the bulk of tetragonal ZrO_2 (101)

This case, and the one discussed in the next session, can be considered hypothetical and are presented here for completeness. In fact, we discuss below what happens if the Ce^{3+} dopant is not on the surface of zirconia, but it lies in the inner layers. The calculations have shown that Ce prefers to stay on the surface of the zirconia particles, and given the high thermal treatment their concentration should be significantly higher than that of bulk Ce^{3+} ions.

Here we consider the case where two Ce^{3+} are buried in the bulk of ZrO_2 (101). The interaction of O_2 shows significant differences with respect to the previous case (Ce^{3+} species on the surface). Also here we observe the formation of a superoxide radical ion, but of course this is adsorbed on top of a surface Zr^{4+} ion.

This adduct has a binding energy of -0.72 eV. We also found another, less stable, chemisorption state with a binding energy of -0.55 eV (Figure 8c). Both chemisorption adducts are associated to an electron transfer, according to reaction 1.

The most stable adduct is associated to a bent configuration with an O-O-Zr angle of 76° , and Zr-O distances of 2.13 Å and 2.24 Å, Figure 8b. The O-O distance is 1.36 Å, compatible with O_2^\bullet configuration, and slightly larger than that reported in previous section for the side-on adduct (1.33 Å). The two oxygen atoms are magnetically non-equivalent, although the difference is small. The

binding energy of this $\text{Zr}^{4+}\text{-O}_2^{\bullet-}$ adduct (-0.72 eV) is very similar to the case where one Ce^{3+} is on the surface but the complex forms on a surface Zr^{4+} ion (-0.65 eV).

The different adsorption mode of $\text{O}_2^{\bullet-}$ on the Zr^{4+} ion, Figure 8, compared to the case discussed above of direct bonding to a surface Ce^{4+} ion can be explained with a different extension of the Zr 4d orbitals compared to the Ce 4f orbitals. This allows a better overlap of the Zr 4d states with the O_2 $2\pi^*$ MO, resulting in a partial covalent and directional bond that results in the tilt angle.

The second adduct, less stable (binding energy -0.55 eV), is very different from the previous one. First, it assumes a bent structure on a Zr^{4+} ion, Figure 8c, in which the oxygen atoms are magnetically non-equivalent, contributing with spin populations 0.45 and 0.67, for a total of 1.12. The O-O-Zr angle of the bent structure is 121° , with a Zr-O distance of 2.31 Å. Moreover, also the O-O distance is different, being 1.29 Å. The lower value of the O-O distance indicates that the electron transfer is not complete and that the bonding has a significant covalent character.

An important difference between the case where Ce^{3+} dopants are at the surface or in the bulk of the zirconia particles is related to the mechanism of the charge transfer. In the first case, the direct, although weak overlap of the Ce and O_2 wave functions justifies the occurrence of the electron transfer. In the second case, the large distance between the O_2 molecule and the dopant implies that a different mechanism must be invoked in order to observe the charge transfer. The DFT calculations, related to the ground state of the system at zero Kelvin, only provide the thermodynamically most favorable configuration, but cannot predict how the electron migrates from a bulk Ce^{3+} ion to the surface (hopping, thermal diffusion, etc.). One cannot exclude that only surface Ce^{3+} ions are effective in determining the charge transfer. This would also explain why only symmetric EPR signals are seen for the two O atoms of the molecule, as this is the preferred configuration assumed in this case.

3.5.3) O_2 adsorption: Ce^{3+} species in the bulk and on the subsurface layer of tetragonal ZrO_2 (101).

We now move to the last model, a Ce^{3+} species buried in an inner (bulk) slab, and a second Ce^{3+} dopant in the subsurface layer of ZrO_2 (101). This model is an intermediate case between those discussed above. The overall picture is very similar to that of two Ce^{3+} ions in the bulk; in fact, the chemisorption of O_2 leads to a bent structure bound to a surface Zr^{4+} ion, Fig. 8b. The binding energy is -0.54 eV (-0.72 eV in the model with two bulk Ce^{3+} ions). Thus, both models displaying a bent structure have larger binding energy (-0.54 eV and -0.72 eV), than the side-on configuration on surface Ce^{3+} ion (-0.45 eV). The bent structure (not reported) is almost the same as in the previous case (Figure 8b), O-O-Zr 76° , O-O distance is 1.36 Å.

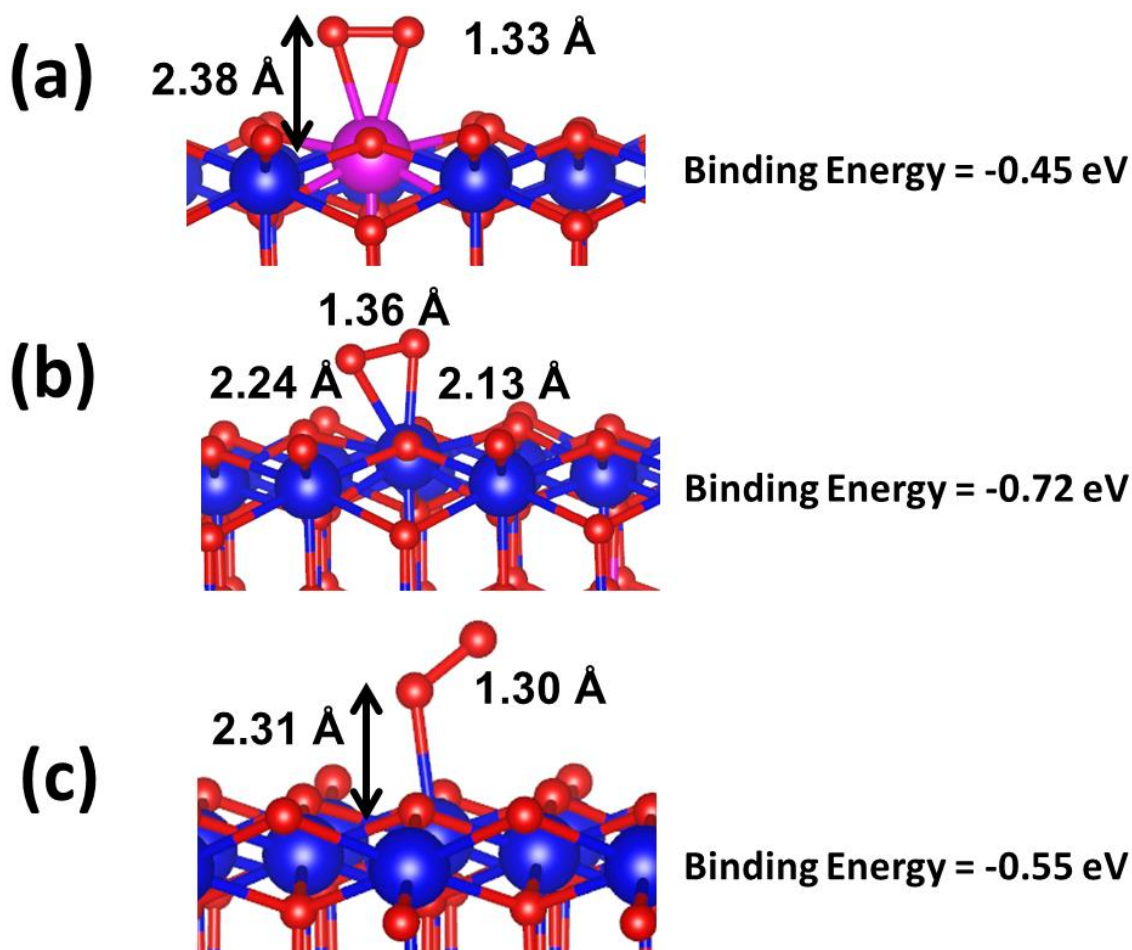


Figure 8: Optimized models obtained by interaction of Ce-doped (101) ZrO_2 surface with O_2 . (a) One dopant is located in the bulk and the second one is located in the surface layer. (b) and (c) bent configurations of O_2 interacting with ZrO_2 with two Ce doping species in the bulk of the model. Magenta: Ce; blue: Zr; red: O.

4. Discussion and conclusive remarks

XRD characterization indicates that a solid solution of Ce ions in ZrO₂ has been obtained in the range of molar concentration between 0.5% and 10%. Evidence of CeO₂ segregation was not observed in the XRD patterns (Fig. 1). In the case of lower loading, even though the identification in the XRD patterns of tiny amount of CeO₂ phase could be difficult, the observed change of the lattice parameters proportional to Ce loading further confirms the formation of a solid solution. Parallel modifications of the lattice parameters are also predicted by the computational study. The DFT results however clearly shows that such a change of lattice parameters should occurs for both the ZrO₂ polymorphs (tetragonal and monocline), while the experimental evidence indicates a significant expansion in the case of the tetragonal structure only, while the lattice of the monoclinic one remains almost unaltered. This suggests that Ce ions are distributed only in the lattice of the tetragonal phase of the synthesized samples and that they are not present in the monoclinic lattice.

It is also worth to mention that this different distribution of Ce ions between the two polymorphs can entail some inhomogeneity in the prepared samples making difficult to establish the real concentration of the dopant in the single polymorph. Such an inhomogeneity can contribute to justify the difference in the percentage of deviations of the lattice parameters ($\Delta\%$ in Table 1), between the prepared samples and the calculated models, which is higher in the case of the real samples.

The agreement between theoretical outputs and experimental evidence about the effect of O₂ adsorption on the surface of Ce-doped ZrO₂ is also convincing. Oxygen adsorption on the activated (oxidized) Ce-ZrO₂ sample leads to an interaction with surface Ce³⁺ ions (reaction 1) leading to the formation of superoxide species adsorbed side-on on top of Ce⁴⁺ ions (Fig.s 3 and 4). The described electron transfer is almost complete being the total spin density on the O₂ molecule about 0.9, in agreement with theoretical predictions. The presence of paramagnetic Ce³⁺ ions cannot be directly monitored by EPR because they are EPR silent in the temperature range covered by our

experiments. However, the presence of trivalent cerium in Ce-ZrO₂ is well-established not only as a consequence of the experiments of superoxide formation here reported but also on the basis of XPS measurements.^{7,11,40} In the present work, moreover, the presence of trivalent cerium species at the surface is supported by the theoretical calculations that find a higher stability for this configuration compared to having the dopants in the bulk.

The original feature of the reported phenomenon is its pressure dependence at room temperature (and even at lower temperatures) indicating a reversible behaviour of the adsorption, typical of a so-called oxygen carrier. This implies the onset of a relatively weak interaction between the molecule and the adsorbing centre. Interestingly, the structure of the oxygen adduct is η^2 (side-on) whereas in most cases of oxygen carriers the structure is end-on. Also these two features are consistent with the DFT calculations that indicate a binding energy of -0.45 eV for a symmetric side-on superoxide. The binding energy (equivalent to about 42 kJ/mol) and the activation energy of desorption are, in fact, typical of reversible chemisorptive phenomena, with relatively fast kinetics of the adsorption-desorption processes⁴⁹.

The calculations show that when the Ce³⁺ ions are in subsurface lattice sites the electron transfer and surface electron scavenging by O₂ also occurs, and the superoxide stabilisation takes place at a Zr⁴⁺ site with stronger interaction energy and slightly asymmetric geometry. This behaviour recalls what observed in the case of thermal annealing at high temperature where a fraction of the superoxide anion is irreversibly bind to surface Zr⁴⁺ ions. For a high level of reduction of the oxide matrix, in fact, it is reasonable to imagine that the transfer of electrons originally formed in the bulk to the oxygen molecule also occurs through zirconium ions at the surface. The ¹⁷O spectrum of such species (not reported for sake of brevity) shows again a structure compatible with a symmetric side-on structure or, at least, with a tiny non-equivalence of the two oxygen atoms as indicated by the calculations.

To conclude, the present work, reports a thorough description of the phenomenon of reversible O₂ adsorption occurring at room temperature and at lower temperature on the surface of Ce-doped ZrO₂. Such a phenomenon is strictly related to the presence of reduced Ce³⁺ ions on the surface of the solid which spontaneously transfer the electron spin density on the oxygen when the molecule is in the proximity of the surface. The so formed Ce⁴⁺-O₂^{•-} adduct can be easily broken by raising the temperature or pumping gaseous oxygen from the atmosphere. The observed behaviour is the same as in the case of oxygen transport systems. Systematic quantitative experiments are planned to verify the possibility of practical application of the described system in the field of gas mixture separations.

Supporting Information

Optimized structure of Ce doped ZrO₂ and charge modification, before and after O₂ adsorption, obtained via Bader analysis. Rietveld refinement of the XRD data.

Acknowledgments

The work has been supported by the Italian MIUR through the PRIN Project 2015K7FZLH SMARTNESS "Solar driven chemistry: new materials for photo- and electro-catalysis".

References

- ¹ Korsvik, C.; Patil, S.; Seal, S.; Self, W.T. Superoxide Dismutase Mimetic Properties Exhibited by Vacancy Engineered Ceria Nanoparticles. *Chem. Comm.* **2007**, 1056-1058.
- ² Xu C.; Qu, X. Cerium Oxide Nanoparticle: a Remarkably Versatile Rare Earth Nanomaterial for Biological Applications, *NPG Asia Materials* **2014**, *6*, e90.
- ³ Li, P.; Chen, X.; Li, Y.; Schwank, J. W. A Review on Oxygen Storage Capacity of CeO₂-Based Materials: InfluenceF, Measurement Techniques, and Applications in Reactions Related to Catalytic Automotive Emissions Ccontrol. *Cat. Today* **2019**, *327*, 90-115.
- ⁴ Fornasiero, P.; Dimonte, R.; Rao, G.R.; Kaspar, J.; Meriani, S.; Trovarelli, A.; Graziani, M. Rh-Loaded CeO₂-ZrO₂ Solid Solution as Highly Efficient Oxygen Exchanger: Dependence of the Reduction Behavior and the Oxygen Storage Capacity on the Structural Properties. *J. Catal.* **1995**, *151*, 168-177.
- ⁵ Di Monte, R.; Kaspar, J. On the Role of Oxygen Storage in Three-Way Catalysis, *Top. Catal.* **2004**, *28*, 47-57.
- ⁶ Paksoy, A.I.; Caglayan, B.S.; Aksoylu, A.E. A Study on Characterization and Methane Dry Reforming Performance of Co-Ce/ZrO₂ Catalyst, *Appl. Catal. B: Environ.* **2015**, *168-169*, 164-174.

- ⁷ Damyanova, S.; Pawelec, B.; Arishtirova, K.; Martinez Huerta, M.V.; Fierro, J.L.G. The Effect of CeO₂ on the Surface and Catalytic Properties of Pt/CeO₂-ZrO₂ Catalysts for Methane Dry Reforming. *Appl. Catal. B: Environ.* **2009**, *89*, 149-159.
- ⁸ Palma, V.; Pisano, D.; Martino, M. Structured Noble Metal-Based Catalysts for the WGS Process Intensification. *Int. J. Hydrogen Energ.* **2018**, *43*, 11745-11754.
- ⁹ Ruettinger, W.; Liu, X.; Farrauto, R. J. Mechanism of Aging for a Pt/CeO₂-ZrO₂ Water Gas Shift Catalyst. *Appl. Catal. B: Environ.* **2006**, *65*, 135-141.
- ¹⁰ Tang, C.; Zhang, H.; Dong, L. Ceria-Based Catalysts for Low-Temperature Selective Catalytic Reduction of NO with NH₃. *Catal. Sci. Technol.* **2016**, *6*, 1248-1264.
- ¹¹ Yu, J.; Si, Z.; Chen, L.; Wu, X.; Weng, D. Selective Catalytic Reduction of NO_x by Ammonia Over Phosphate-Containing Ce_{0.75}Zr_{0.25}O₂ solids. *Appl. Catal. B: Environ.* **2015**, *163*, 223-232.
- ¹² Gionco, C.; Giamello, E.; Mino, L.; Paganini, M.C., The Interaction of Oxygen with the Surface of CeO₂-TiO₂ Mixed Systems: An Example of Fully Reversible Surface-to-Molecule Electron Transfer. *Phys. Chem. Chem. Phys.* **2014**, *16*, 21438-21445.
- ¹³ Polliotto, V.; Livraghi, S.; Agnoli, S.; Granozzi, G.; Giamello, E. Reversible Adsorption of Oxygen as Superoxide Ion on Cerium Doped Zirconium Titanate. *Appl. Catal. A: General* **2019**, *580*, 140-148.
- ¹⁴ Li, J.-R.; Sculley, J.; Zhou, H.-C. Metal-Organic Frameworks for Separations. *Chem. Rev.* **2012**, *112*, 869-932.
- ¹⁵ Tian, F.; Zhang, X.; Chen, Highly Selective Adsorption and Separation of Dichloromethane/Trichloromethane on a Copper-Based Metal-Organic Framework Y. *RSC Adv.* **2016**, *6*, 31214-31224.
- ¹⁶ Giamello, E.; Sojka, Z.; Che, M.; Zecchina, A. Spectroscopic Study of Superoxide Species Formed by Low-Temperature Adsorption of Oxygen onto Cobalt Oxide (CoO)-Magnesium Oxide Solid Solutions: an Example of Synthetic Heterogeneous Oxygen Carriers. *J. Phys. Chem.* **1986**, *90*, 6084-6060.
- ¹⁷ Sojka, Z.; Giamello, E.; Che, M.; Zecchina, A.; Dyrek, K. Electronic Structure and Orientation of Dioxygen Species on the Surface of Cobalt Monoxide-Magnesium Oxide Solid Solutions. *J. Phys. Chem.* **1988**, *92*, 1541-1547.
- ¹⁸ Siedl, N.; Gügel, P.; Diwald, O. First Combined Electron Paramagnetic Resonance and FT-IR Spectroscopic Evidence for Reversible O₂ Adsorption on In₂O_{3-x} Nanoparticles. *J. Phys. Chem. C* **2013**, *117*, 20722-20729.
- ¹⁹ Gideoni, M.; Steinberg, M. The Study of Oxygen Sorption on Cerium(IV) Oxide by Electron Spin Resonance. *J. Solid State Chem.* **1972**, *4*, 370-373.
- ²⁰ Gideoni, M.; Kautherr, N.; Steinberg, M. An ESR Study of ¹⁷O₂ on Cerium(IV) Oxide. *Isr. J. Chem.* **1974**, *12*, 1069-1073.
- ²¹ Che, M.; Kibblewhite, J.F.J.; Tench, A.J.; Dufaux, M.; Naccache, C. Oxygen Species Adsorbed on CeO₂/SiO₂ Supported Catalysts. *J. Chem. Soc. Faraday Trans. I* **1973**, *69*, 857-863.
- ²² Lutterotti, L.; Matthies, S.; Wenk, H.R.; Schultz A.S.; Richardson, J.W. Combined Texture and Structure Analysis of Deformed Limestone from Time-of-Flight Neutron Diffraction Spectra. *J. Appl. Phys.* **1997**, *81*, 594-600.
- ²³ <http://maud.radiographema.com>
- ²⁴ Kresse, G.; Hafner, J. Ab Initio Molecular Dynamics for Liquid Metals. *Phys. Rev. B* **1993**, *47*, 558-561.
- ²⁵ Kresse, G.; Hafner, J. Ab Initio Molecular-Dynamics Simulation of the Liquid-Metal-Amorphous-Semiconductor Transition in Germanium. *Phys. Rev. B* **1994**, *49*, 14251-14269.
- ²⁶ Kresse, G.; Furthmüller, J. Efficiency of Ab-Initio Total Energy Calculations for Metals and Semiconductors Using a Plane-Wave Basis Set. *Comput. Mater. Sci.* **1996**, *6*, 15-50.
- ²⁷ Kresse, G.; Furthmüller, J. Efficient Iterative Schemes for Ab Initio Total-Energy Calculations Using a Plane-Wave Basis Set. *Phys. Rev. B* **1996**, *54*, 11169-11186.
- ²⁸ Kresse, G.;

- Joubert, D. From Ultrasoft Pseudopotentials to the Projector Augmented-Wave Method. *Phys. Rev. B* **1999**, *59*, 1758–1775.
- ²⁹ Perdew, J. P.; Burke, K.; Ernzerhof, M. Generalized Gradient Approximation Made Simple. *Phys. Rev. Lett.* **1996**, *77*, 3865–3868.
- ³⁰ Dudarev, S. L.; Botton, G. A.; Savrasov, S. Y.; Humphreys, C. J.; Sutton, A. P. Electron-Energy-Loss Spectra and the Structural Stability of Nickel Oxide: An LSDA+U Study. *Phys. Rev. B* **1998**, *57*, 1505–1509.
- ³¹ Migani, A.; Vayssilov, G. N.; Bromley, S. T.; Illas, F.; Neyman, K. M. Greatly Facilitated Oxygen Vacancy Formation in Ceria Nanocrystallites. *Chem. Commun.* **2010**, *46*, 5936–5938.
- ³² Loschen, C.; Carrasco, J.; Neyman, K. M.; Illas, F. First-Principles *Phys. Rev. B* **2007**, *75*, 035115.
- ³³ Bruix, A.; Rodriguez, J. A.; Ramírez, P. J.; Senanayake, S. D.; Evans, J.; Park, J. B.; Stacchiola, D.; Liu, P.; Hrbek, J.; Illas, F. A New Type of Strong Metal–Support Interaction and the Production of H₂ through the Transformation of Water on Pt/CeO₂ (111) and Pt/CeOx/TiO₂ (110) Catalysts. *J. Am. Chem. Soc.* **2012**, *134*, 8968–8974.
- ³⁴ Thang, H. V.; Tosoni, S.; Fang, L.; Bruijninx, P.; Pacchioni, G. Nature of Sintering-Resistant, Single-Atom Ru Species Dispersed on Zirconia-Based Catalysts: A DFT and FTIR Study of CO Adsorption. *ChemCatChem* **2018**, *10*, 2634–2645.
- ³⁵ Bouvier, P.; Djurado, E.; Ritter, C.; Dianoux, A.; Lucazeau, G. Low Temperature Phase Transformation of Nanocrystalline Tetragonal ZrO₂ by Neutron and Raman Scattering Studies. *Int. J. Inorg. Mater.* **2001**, *3*, 647–654.
- ³⁶ Howard, C. J.; Hill, R. J.; Reichert, B. E. Structures of ZrO₂ Polymorphs at Room Temperature by High-Resolution Neutron Powder Diffraction. *Acta Crystallogr. Sect. B Struct. Sci.* **1988**, *44*, 116–120.
- ³⁷ Tosoni, S.; Sauer, J. Accurate Quantum Chemical Energies for the Interaction of Hydrocarbons with Oxide Surfaces: CH₄/MgO(001). *Phys. Chem. Chem. Phys.* **2010**, *12*, 14330.
- ³⁸ Damyanova, S.; Pawelec, B.; Arishtirova, K.; Martinez Huerta, M.V.; Fierro, J.L.G. Study of the Surface and Redox Properties of Ceria–Zirconia Oxides. *App. Catal. A: General* **2008**, *337*, 86–96.
- ³⁹ Di Monte, R.; Kaspar, J. Nanostructured CeO₂–ZrO₂ mixed oxides. *J. Mater. Chem.* **2005**, *15*, 633–648.
- ⁴⁰ Alifanti, M.; Baps, B.; Blangenois, N.; Naud, J.; Grange, P.; Delmon, B. Characterization of CeO₂–ZrO₂ Mixed Oxides. Comparison of the Citrate and Sol–Gel Preparation Methods. *Chem. Mater.* **2003**, *15*, 395–403.
- ⁴¹ Gionco, C.; Paganini, M.C.; Giamello, E.; Sacco, O.; Vaiano, V.; Sannino, D. Rare Earth Oxides in Zirconium Dioxide: How to Turn a Wide Band Gap Metal Oxide into a Visible Light Active Photocatalyst. *J. Energy Chem.* **2017**, *26*, 270–276.
- ⁴² Anpo, M.; Che, M.; Fubini, B.; Garrone, E.; Giamello, E.; Paganini, M.C.; Generation of Superoxide Ions at Oxide Surfaces. *Top. Catal.* **1999**, *8*, 189–198.
- ⁴³ Kanzig, M.; Cohen, M. H. Paramagnetic Resonance of Oxygen in Alkali Halides *Phys. Rev. Letters* **1959**, *3*, 509–510.
- ⁴⁴ Pietrzyk, P.; Podolska, K.; Mazur, T.; Sojka, Z. Heterogeneous Binding of Dioxygen: EPR and DFT Evidence for Side-On Nickel(II)–Superoxo Adduct with Unprecedented Magnetic Structure Hosted in MFI Zeolite. *J. Am. Chem. Soc.* **2011**, *133*, 19931–19943.
- ⁴⁵ Chiesa, M.; Giamello, E.; Paganini, M.C.; Sojka, Z.; Murphy, D.M. Continuous Wave Electron Paramagnetic Resonance Investigation of the Hyperfine Structure of ¹⁷O₂⁻ Adsorbed on the MgO Surface. *J. Chem. Phys.* **2002**, *116*, 4266–4274.
- ⁴⁶ Niederhoffer, E.C.; Timmons, J.H.; Martell, A.E. Thermodynamics of Oxygen Binding in Natural and Synthetic Dioxygen Complexes. *Chem. Rev.* **1984**, *84*, 137–203.
- ⁴⁷ Giamello, E.; Volante, M.; Fubini, B.; Geobaldo, F.; Morterra, C. An EPR Study on the Formation of the Superoxide Radical Ion on Monoclinic Zirconia. *Mat. Chem. Phys.* **1991**, *29*, 379–386.

⁴⁸ Preda, G.; Migani, A.; Neyman, K. M.; Bromley, S. T.; Illas, F.; Pacchioni, G. Formation of Superoxide Anions on Ceria Nanoparticles by Interaction of Molecular Oxygen with Ce³⁺ Sites. *J. Phys. Chem. C* **2011**, *115*, 5817–5822.

⁴⁹ Bolis, V.; Fubini, B.; Giamello, E.; Reller A. Effect of form of the Surface Reactivity of Differently Prepared Zinc Oxides. *J. Chem. Soc. Faraday Trans I*, **1989**, *85*, 855-867.

TOC Graphic

